ELSEVIER

Journal of Alloys and Compounds 423 (2006) 102–106

Journal of ALLOYS AND COMPOUNDS

www.elsevier.com/locate/jallcom

Formation and characterization of nanocrystalline binary oxides of yttrium and rare earths metals

Giora Kimmel [a,*], Jacob Zabicky [a], Elena Goncharov [a], Dmitry Mogilyanski [a], Arie Venkert [b], Yishai Bruckental [c], Yosef Yeshurun [c]

[a] *The Institutes for Applied Research, Ben-Gurion University of the Negev, 84105 Beer-Sheva, Israel*
[b] *Physics Department, Nuclear Research Center Negav, Beer-Sheva, Israel*
[c] *Department of Physics, Bar-Ilan University, Ramat-Gan, Israel*

Available online 8 February 2006

Abstract

Binary oxides of yttrium (Y) and rare earths (R) are used for their varied chemical and physical (e.g., optical and dielectric) properties. Coprecipitated xerogels, which are mixtures of hydroxides and oxides of Y and R, were thermally annealed in air at constant temperatures in the range from 100 to 1400 °C for 3 h. The lowest temperature at which a pure oxide is obtained varies with composition. The binary oxides of Y(III) and R(III) afford ideal solid solutions with chemical formula $(R_xY_{1-x})_2O_3$, where the unit cell parameters are a linear function of the atomic ratio $x = R/(R + Y)$, obeying Vegard's law. However, the range of solubility was dependent on the composition and temperature of formation. In the case of binary Y(III)–R(IV) oxides, of general formula $(R_xY_{1-x})_2O_{3+x}$, two ranges of solubility were clearly identified: in the system of Y–Pr oxides a solubility gap was found between these ranges, whereas in the case of Ce–Y oxides the solutions were found by XRD and TEM to be coherent, without a solubility gap. XRD line broadening analysis points to line broadening as being mainly due to small crystallite size, whereas the contribution of microstrain to line broadening is negligible. The magnetic properties are strongly dependent on the particle size. Nanocrystalline Sm(III) oxide and the $SmYO_3$ solid solution formed at 900 °C are paramagnetic; however, superparamagnetism was found for the same compounds with larger grain size, formed at 1200 °C, for both cubic and monoclinic structures.

Keywords: Nanostructured materials; Oxide materials; X-ray diffraction

1. Introduction

Binary oxides of yttrium and rare earths are used for their optical [1], dielectric [2,3] and other chemical and physical properties [4–6]. Whereas Y_2O_3 has always the Mn_2O_3 type *cI*80 cubic structure, the pure rare earths oxides have structures such as the La_2O_3 type monoclinic, *hP*5 hexagonal, the Sm_3O_4 type *cI*84 cubic, the Sm_2O_3 type *mC*30 monoclinic, and the fluorite (CaF_2) type *cF*8 cubic [7]. Therefore, formation of a single phase as a solid solution between yttria and a rare earth oxide is not certain. It was decided to investigate the phase diagrams of yttria and rare earth oxide binary alloys at temperatures below 1200 °C, since the data on these compositions are rather scant. The sol–gel technique affords an easy way for preparing a variety of compositions and crystalline sizes in the low to the high nanoscale range [8]. The main objective of the present work was to explore the following items, which show interesting characteristics for the behavior of nanocrystalline yttrium–rare earth binary oxides, synthesized between 100 and 1400 °C: (a) kinetics of oxide formation from the xerogels, (b) crystal structure, (c) unit cell parameters, (d) grain size, (e) microstrain and (f) magnetic properties. X-ray powder diffracrion (XRPD) and transmission electron microscopy (TEM) were the main experimental means for items (a)–(e).

2. Experimental

2.1. Oxide preparation

The starting materials were water-soluble yttrium (Y) and rare earth (R = Ce, Pr, Nd, Sm, Gd and Dy) salts. A magnetically stirred solution containing Y(III) and R(III) ions in the desired atomic fraction ($x = R/(R + Y) = 0$, 1/10, 1/5, 1/3, 2/5, 1/2, 3/5, 2/3, 4/5, 9/10 and 1) was brought to alkaline pH on dropwise adding concentrated ammonia. The precipitated gels were filtered and washed several times and let to dry in air. The xerogels were calcined in air for 3 h, in a furnace

* Corresponding author. Tel.: +972 8 646 9075; fax: +972 8 690 9450.
E-mail address: kimmel@bgu.ac.il (G. Kimmel).

0925-8388/$ – see front matter © 2006 Elsevier B.V. All rights reserved.
doi:10.1016/j.jallcom.2005.12.037

at fixed temperatures between 100 and 1400 °C and quenched by rapidly cooling on taking them out from the furnace.

2.2. Characterization

All samples were analyzed by X-ray diffraction. The XRD system consisted of a Huber Guinier digitized camera with a Fuji imaging plate detector, a rotating Cu anode and an incident beam monochromator serving as pure $K\alpha_1$ source. Rietveld's method [9–11] was applied, using the public domain programs *DBWS* for refinement of the crystal data (atomic positions and cell parameters), *FullProf* (mostly for graphic presentation) and *Rietquan* for strain and size evaluation. Some samples were observed by TEM (JEOL's JEM-2010 at 200 kV) and by SEM/EDS (Noran). Magnetic properties were measured for some oxides of the Sm–Y system, using a Quantum Design MPMSXL SQUID magnetometer. Magnetization was measured at constant temperature as a function of the external field being swept from 20 kOe down to −20 kOe and back to 20 kOe. This procedure was repeated at different temperatures. In addition, magnettization was measured at 1 kOe as a function of the temperature being swept from 15 K up to 300 K and back to 15 K.

3. Results and discussion

3.1. Structure and microstructure

The structure of the pure oxides was dependent on the temperature of thermal annealing. According the phase rule, for a single component sharp phase transitions are expected when the temperature changes. However, single-component materials with more than one phase were sometimes obtained, pointing to a system still far from thermal equilibrium. The studied xerogels have a threshold annealing temperature for total conversion into oxides. Furthermore, as thermal annealing was carried out in air, in some of the original xerogels R(III) oxides underwent oxidation to R(IV) oxides.

3.1.1. Pure oxides

Yttria showed a *cI*80 cubic structure from 600 to 1400 °C [7]. From the rare earths investigated, only Dy_2O_3 and Yb_2O_3 were isomorphous with yttria over all this temperature range, Gd_2O_3 from 600 to1200 °C, Sm_2O_3 from 700 to 800 °C and Pr_2O_3 when it was formed at 1200 °C by thermal decomposition of a higher oxide. R_2O_3 species adopting the monoclinic *mC*30 structure were Gd_2O_3 at 1300 °C, Sm_2O_3 from 900 to 1200 °C and Nd_2O_3 from 700 to 900 °C, turning into the hexagonal structure *hP*5 when calcined at 1000 °C. CeO_2 was already formed at the xerogel stage and had the fluorite *cF*12 structure over the whole investigated temperature range. A higher oxide of Pr showed the fluorite structure from 500 to 1100 °C.

Most oxides prepared above 700 °C were obtained as well crystallized materials with crystal data similar to bulk published results [7]. The 547 pm unit cell parameter of a higher Pr oxide pointed to composition Pr_6O_{11} [12] rather than PrO_2. Oxides prepared by thermal annealing of the xerogel in the lower temperature range were nanocrystalline, accompanied with line broadening and line shifts of their XRD. Fig. 1 shows the grain size versus the annealing temperature for Y_2O_3, as obtained from XRD line broadening analysis [11]. It was found that the line broadening should be attributed mainly to the grain size, as the microstrain usually was less than 0.01%. The XRD results

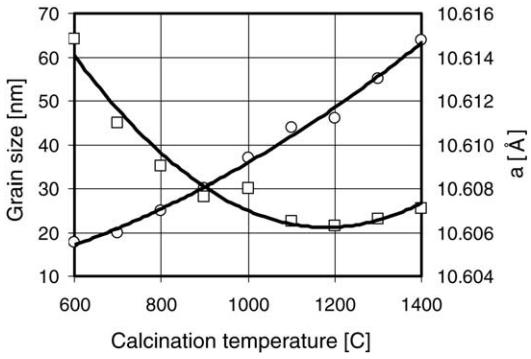

Fig. 1. Dependence of the grain size (◯) and the cell parameter *a* (□) on the calcination temperature of the xerogel precursor of Y_2O_3.

were supported by TEM observations. Thus, for example, XRD line broadening analysis yielded crystal size of 52 nm for the Pr oxide (fluorite structure) formed at 700 °C during 3 h, which is in the range of the TEM images shown in Fig. 2. A trend of decreasing unit cell parameters with increasing annealing temperature was observed for all the investigated phases and also for pure oxides, as shown in Fig. 1 for Y_2O_3. This generalizes published work for CeO_2, correlating the increase of the unit cell parameter with the grain size when it decreases below 20 nm [13]. The usual explanation for this effect is the increasing weight of the surface properties in nanocrystalline phases. An alternative model is based on the real ionic bond model for finite numbers of ion pairs. More details on this phenomenon will be published elsewhere.

3.1.2. Binary oxides

The binary Y_2O_3–R_2O_3 system forms solid solutions of formula $(Y_{1-x}R_x)_2O_3$ in a wide range of compositions. However,

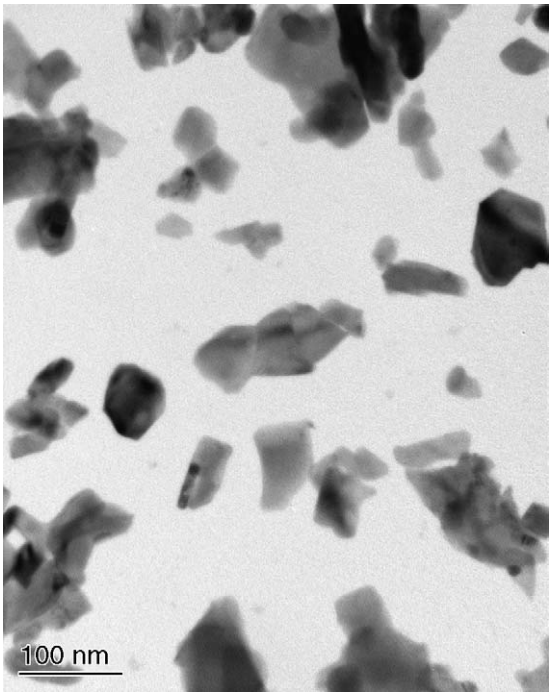

Fig. 2. TEM image of Pr oxide (fluorite structure) formed at 700 °C during 3 h.

Table 1
Y_2O_3–R_2O_3 solid solutions: solubility ranges

R	Temperature of formation (°C)	Cubic Y_2O_3-like, $x = R/(R+Y)$	Monoclinic Sm_2O_3-type, $x = R/(R+Y)$
Dy, Yb	700–1400	0–1	–
Gd	700–1200	0–1	–
Gd	1300	0–0.9	1
Sm	700	0–1	–
Sm	900	0–0.9	1
Sm	1200	0–0.66	0.8–1
Nd	900	0–0.66	0.8–1
Nd	1200	0–0.5	0.66–1

Composition ranges for the appearance of different phase types.

the solubility range depends on the crystal structure of the R_2O_3 oxides. In spite of the differences in the crystal structure sometimes found for the pure oxide, the cubic Mn_2O_3 type (Y_2O_3-like) dominates most alloys (see Table 1). The unit cell parameters of alloys prepared at a fixed temperature showed a linear dependence on the atomic ratio $x = R/(R+Y)$, obeying Vegard's law, as shown in Fig. 3. The excellent accord to Vegard's law shown by Dy, Gd and Yb in this figure does not apply to Nd, which shows a nonlinear dependence ($a = 0.0368x^2 + 0.4449x + 10.606$, $0 \le x \le 0.8$; $R^2 = 0.9992$).

The molecular formula for binary oxides containing Y(III) and R(IV) elements, providing the charge balance, can be expressed as $(Y_{1-x}R_x)_2O_{3+x}$ or $(Y_{1-x}R_x)O_{1.5+0.5x}$. These formulas can emulate, respectively, the metallic element contents of Y_2O_3, requiring an additional site for oxygen ions [14], or that of PrO_2 or CeO_2, implying oxygen vacancies in the fluorite structure. In the Y–Ce and Y–Pr oxide systems two ranges of solid solutions were found, clearly denoted by the functional dependence of the cell parameter on the atomic fraction $x = R/(R+Y)$ (Table 2). However, in the Y–Pr system there is a solubility gap between the Y-rich and the Pr-rich solutions where a mixture of two phases appears (Fig. 4). The structure refinement from the XRD data resulted in a mixture of two phases, one is a Y_2O_3-like structure and the other is fluorite-like structure. The Rietveld refinement of the structures for $x = 0.67$ is shown in Fig. 5.

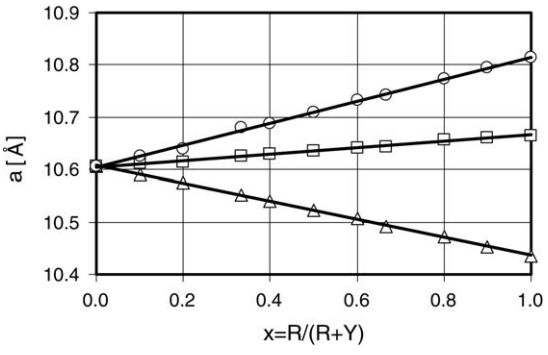

Fig. 3. Dependence of the cell parameter a on the atomic ratio x, for solid solutions of binary R(III)–Y oxides, prepared by calcination of coprecipitated xerogels at 900 °C for 3 h. (◯) R = Gd ($a = 0.211x + 10.604$; $R^2 = 0.9983$); (□) R = Dy ($a = 0.0609x + 10.605$; $R^2 = 0.9952$); (△) R = Yb ($a = -0.1708x + 10.607$; $R^2 = 0.9997$).

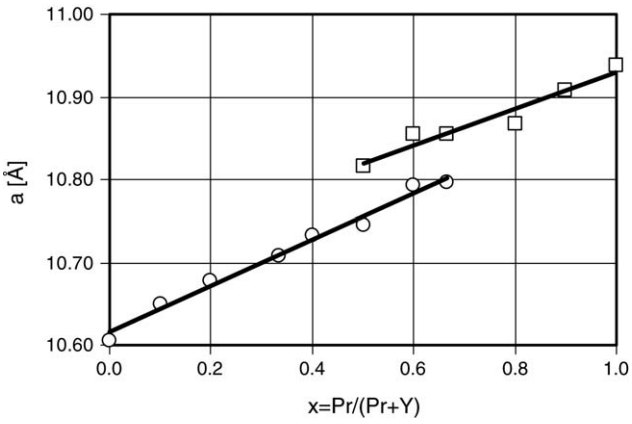

Fig. 4. Dependence of the cell parameter a on the atomic ratio x, for solid solutions of binary Pr–Y oxides, prepared by calcination of coprecipitated xerogels at 1300 °C for 3 h. Note the incoherent transition from Mn_2O_3-type crystals (◯) to fluorite-type crystals (□), and the overlapping region where crystals of both types coexist.

On the other hand, in the Y–Ce system the two solution types are coherent (merging into a single phase) and the transition from one type to the other takes place by changing the slope of the cell parameter versus composition (Fig. 6). High resolution TEM of the binary phase $(Ce_{0.4}Y_{0.6})_2O_{3.4}$ (Fig. 7), at the

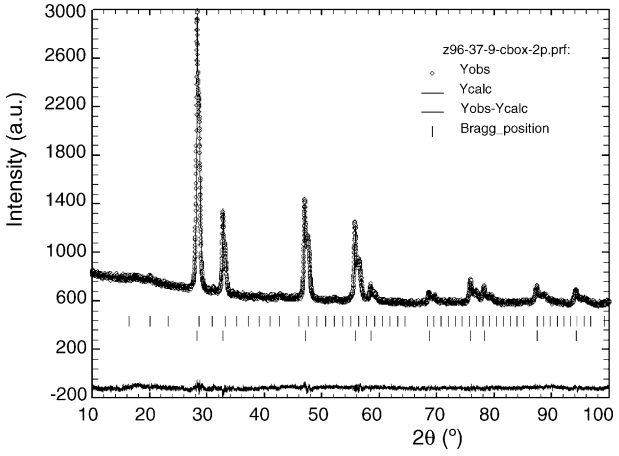

Fig. 5. Rietveld diagram of a mixture of a cubic Y_2O_3-like phase and a fluorite-type phase of binary (Pr and Y) oxides. Pseudo-Voigt profile was assumed. Rp = 17.7, Rwp = 9.82 and Rexp = 22.88.

Table 2
Y_2O_3–R_2O_3 solid solutions: solubility ranges

R	Temperature of formation (°C)	Cubic Mn_2O_3-type, $x = R/(R + Y)$	Cubic CaF_2 type, $x = R/(R + Y)$
Pr	900	0–0.67	0.60–1[a]
Pr	1300	0–0.67	0.50–1[a]
Ce	600	0–0.40	0.40–1
Ce	700	0–1.00	–
Ce	900	0–0.90	1
Ce	1200	0–0.66	0.80–1

Composition ranges for the appearance of different phase types.
[a] The pure oxide appears as Pr_6O_{11} rather than PrO_2.

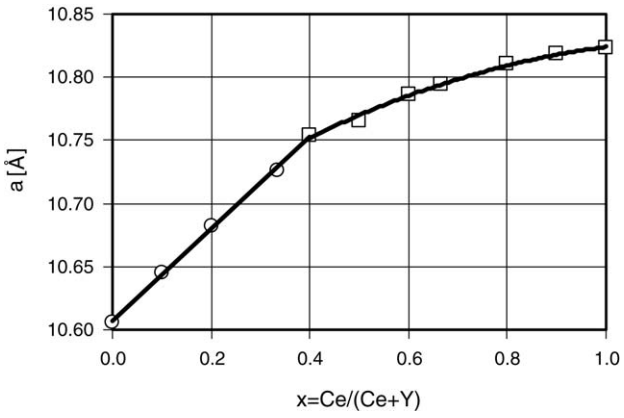

Fig. 6. Dependence of the cell parameter a on the atomic ratio x, for solid solutions of binary Ce–Y oxides, prepared by calcinations of coprecipitated xerogels at 900 °C for 3 h. Note the coherent transition from Mn_2O_3-type crystals (◯) to fluorite-type crystals (□).

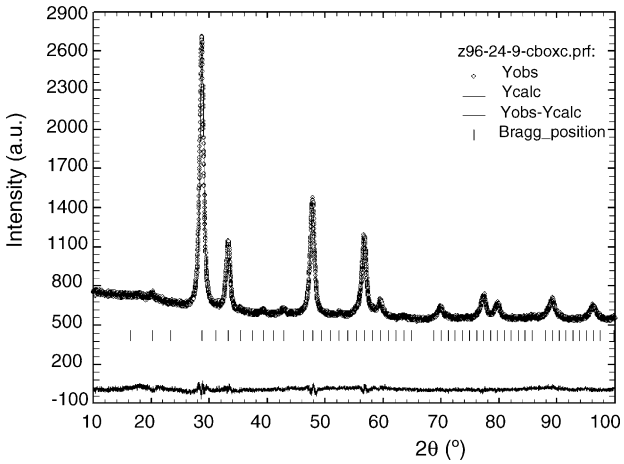

Fig. 8. Rietveld diagram of the binary oxide phase $(Ce_{0.4}Y_{0.6})_2O_{3.4}$. Pseudo-Voigt profile was assumed. Rp = 12.9, Rwp = 8.54, Rexp = 19.83.

intersection of both solution types, shows a unique phase. This is in accordance with the Rietveld diagram of this composition (Fig. 8), also showing a single phase. The refined crystal data for this composition are given in Table 3. Recent published work suggests four distinct regions of behavior for the Y–Ce oxide system, for materials prepared at 1600 °C for 5 days [15]. The discontinuity of the cell parameter's slope showing two separate domains is in partial support of their suggestion. However, more study is needed to find if there are one or more crystal structures among the nanometric phases in the Y_2O_3–CeO_2 system.

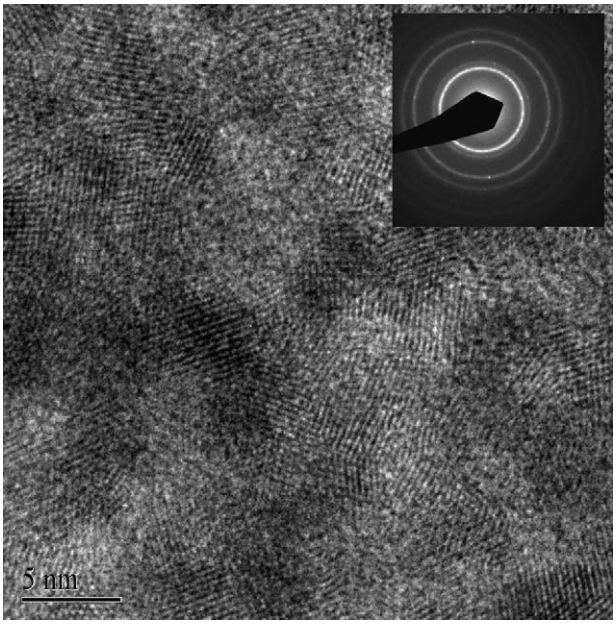

Fig. 7. High resolution TEM image of $(Ce_{0.4}Y_{0.6})_2O_{3.4}$ formed by calcinations of the xerogel at 600 °C during 3 h.

3.2. Magnetic properties

The magnetic properties of Sm_2O_3 and $SmYO_3$ samples prepared at 900 and 1200 °C were studied at magnetic fields up to 20 kOe. All samples show a well developed paramagnetic signal. No effect could be ascribed to the temperature of synthesis

Table 3
Crystal structure of $(Ce_{0.4}Y_{0.6})_2O_{3.4}$ as refined by the Rietveld method ($R_B = 0.06$)[a]

Wyckof	Occupancy	Relative coordinates of asymmetric unit		
		x	y	z
8(b)	$0.4Ce^{4+} + 0.6Y^{3+}$	1/4	1/4	1/4
24(b)	$0.4Ce^{4+} + 0.6Y^{3+}$	0.4847	0	0
48(e)	$1.0O^{2-}$	0.3931	0.1520	0.3814
16(c)	$0.4O^{2-}$	0.3870	0.3870	0.3870

Space group $Ia\bar{3}$ (cubic); cell parameter: 1075.5 pm.
[a] Xerogel annealed for 3 h at 600 °C.

at these relatively low fields. A field increase to 50 kOe caused a change in the magnetic moment of both samples synthesized at 1200 °C, pointing to a superparamagnetic moment being in effect. This behavior was reproducible after changing field or operational temperature, but was not observed for the sample synthesized at 900 °C. It seems that the superparamagnetism depends on the grain size and not on the crystal structure. The magnetic moments were dependent on the Sm concentration, similarly to the behavior of analogous Gd oxides [16].

4. Conclusions

Using the sol–gel technique to produce binary yttrium–rare earth oxides allows exploring the phase diagram at temperatures below 1200 °C. The nanocrystalline alloys produced in this range vary in grain size from 5 to 100 nm and belong to diverse structural types. They show peculiar properties related to the grain size, the rare earth element and the R to Y atomic ratio in the material. The binary Y(III)–R(III) oxides belong mostly to the Mn_2O_3-type of cubic crystals. Y(III)–R(IV) oxides may belong either to this type or to the fluorite type of cubic crystals, depending on whether the alloy is rich in Y(III) or R(IV). The grain size was also found to affect the magnetic properties of Y–Sm oxides, with superparamagnetism appearing in crystals grown at high temperatures.

References

[1] J. Stone, C.A. Burrus, J. Appl. Phys. 49 (1978) 2281–2287.
[2] Y. Baba, K. Eguchi, H. Arai, J. Electrochem. Soc. 135 (1988) 2077–2080.
[3] H. Yahiro, K. Eguchi, H. Arai, Solid State Ionics 36 (1989) 71–75.
[4] P.J.R. Montes, M.E.G. Valerio, M.A. Macêdo, F. Cunha, F.J.M. Sasaki, Microelectron. J. (2003) 557–559.
[5] B. Antic, P. Önnerud, D. Rodic, R. Tellgren, Powder Diffr. 8 (1993) 216–220.
[6] M. Mitric, P. Ommerud, D. Rodic, R. Tellgern, A. Szytula, M.L.J. Napijalo, J. Phys. Chem. Solids 8 (1993) 967–972.
[7] P. Villars, L.D. Calvert, Pearson Handbook of Crystallographic Data for Intermetallic Phases, ASM, USA, 1986.
[8] R. Subramanian, P. Shankar, S. Kavithaa, S.S. Ramakrishnan, P.C. Angelo, H. Venkataraman, Mater. Lett. 48 (2001) 342–346.
[9] H.M. Rietveld, A J. Appl. Cryst. 2 (1969) 65–71.
[10] R.A. Young, J. Appl. Cryst. 28 (1995) 366–367.
[11] L. Lutterotti, P. Scardi, J. Appl. Cryst. 25 (1992) 459–462.
[12] W. Schreiner, International Committee for Diffraction Data, PDF No. 42-1121.
[13] F. Zhang, S.-W. Chan, J.E. Spanier, E. Apak, Q. Jin, R.P. Robinson, I.P. Herman, Appl. Phys. Lett. 80 (2002) 127–129.
[14] N. Gabbtias, J.G. Thompson, R.L. Withers, A.D. Rae, J. Solid State Chem. 115 (1995) 12–36.
[15] R. Wallenberg, R. Withers, D.J.M. Bevan, J.G. Thompson, P. Parlow, B.G. Hyde, J. Less Common. Met. 156 (1989) 1–16.
[16] A.V. Malakhovski, I.S. Edelman, Y. Radzymer, Y. Yeshurun, A.M. Potselukyo, T.V. Zambina, A.V. Zamkov, A.F. Zaitzkev, J. Magn. Magn. Mater. 263 (2003) 161–172.